

Joint Fitting of CLJ1226.9

C. Romero¹*, M. McWilliam^{2,3}, J.-F. Macías-Pérez², and NIKA collaboration

¹ Institut de RadioAstronomie Millimétrique (IRAM), Grenoble, France

² Laboratoire de Physique Subatomique et de Cosmologie, Université Grenoble Alpes, CNRS/IN2P3, 53, avenue des Martyrs, Grenoble, France

³ Imperial College London, Kensington, London SW7 2AZ, UK

Received May 22, 2017 / Accepted –

Abstract

We present non-parametric pressure profiles of galaxy clusters determined from SZ data from the MUSTANG, NIKA, and Bolocam instruments. We note that, despite the differences in angular resolution, observing frequency, and observing strategies, there is generally good agreement. As expected from the effective transfer function of data processing, the ability to recover the pressure profile beyond the field of view of these instruments diminishes rapidly. The overlap in spatial sensitivity of these three datasets ensures consistency on scales $0.05R_{500} < r < 2R_{500}$. Given the weak constraints at the largest radii, we included a prior from Planck on the integrated Compton Y parameter.

Key words. – Galaxies: clusters: individual: CLJ1226.9+3352

1. Introduction

In recent years, Sunyaev Zel’dovich (SZ) effect observations have seen an increase in high resolution ($\theta \lesssim 30''$) observations (e.g. Mason et al. 2010; Adam et al. 2014; Kitayama et al. 2016). These observations come from MUSTANG on the Robert C. Byrd Green Bank Telescope (GBT Dicker et al. 2008), NIKA on the IRAM 30-meter telescope (Monfardini et al. 2010), and ALMA, band 3 observations. However, all of these high resolution instruments have been limited in their ability to recover signal at large scales (beyond $\sim 45'$ asecs for MUSTANG and ALMA, and $\sim 100''$ for NIKA). As galaxy clusters have characteristic radii, $R_{500} \gtrsim 3'$, SZ observations made with these instruments have not been able to recover the entire signal of the observed galaxy clusters. Therefore, observations from SZ instruments which recover SZ at larger scales such as Bolocam Czakon et al. (2015) or Planck (Planck Collaboration et al. 2013b) have been used in Romero et al. (2015) and Adam et al. (2014) respectively.

These joint analyses have shown the ability to constrain the pressure profile of the intracluster medium (ICM) of individual galaxy clusters over a large spatial range, often by assuming some parameterized pressure profile (e.g. Romero et al. 2016; Adam et al. 2014). In Romero et al. (2015), the difference in fitted pressure profiles with the addition of MUSTANG data was noted. In the case of Romero et al. (2016); Adam et al. (2014), the pairs of instruments used did not have an overlap in scales of instrument sensitivity, so the addition of another instrument would not necessarily present any discrepancies. However, as new SZ instruments with sensitivity to a larger range of scales come online (Monfardini et al. 2014; Dicker et al. 2014), there will be overlap, which for clusters observed with multiple instruments, studies of the kinetic SZ effect, or relativistic corrections (Itoh et al. 1998) will be of significant interest and stand to benefit from the additional frequency coverage. To be sure of

the results of these analyses, it will be critical to understand any systematics involved with individual instruments. Recent results combining Bolocam and Planck data (Sayers et al. 2016), which overlap in regions of sensitivity, show non-trivial changes from previous Bolocam-only results (Sayers et al. 2013).

Many SZ analyses thus far have focused on fitting a smooth pressure profile to their data; over a decade ago, the beta model (Cavaliere & Fusco-Femiano 1978) was used. While a self-similar (Mroczkowski et al. 2009) and analytical pressure profile based on a polytropic equation of state (Bulbul et al. 2010) have been explored, the general Navaro-Frenk-and-White (gNFW Nagai et al. 2007) has garnered the most traction, with a fairly canonical set of parameters coming from Arnaud et al. (2010) (Hereafter, A10). While some SZ studies have attempted to deproject their data (e.g. Sayers et al. 2013), and fit pressure profiles to their deprojected data, the publication of non parametric pressure profile constraints have been scarce. Investigating cluster pressure profiles non parametrically will show deviations from the smooth pressure profile, which could be cause either due to systematics or inherent physical perturbations. That is, if we wish to better understand discrepancies between SZ constraints, as discussed previously, investigating the non-parametric fits between instruments will provide a viable route to this end. Independently, understanding perturbations within the cluster itself is also important in the context of using galaxy clusters as cosmological probes.

Counts of galaxy clusters by mass and redshift serve to constrain cosmological parameters, notably Ω_Λ , the amplitude of fluctuations, σ_8 , and the equation of state of dark energy, w . Constraints on these parameters derived from galaxy cluster samples are generally limited by the accuracy of mass estimation of galaxy clusters (e.g. Hasselfield et al. 2013; Reichardt et al. 2013). Scaling relations which relate global (integrated) observables to the cluster mass are often employed. Currently, scaling relations as applied to observables over an intermediate radial region of galaxy clusters is preferred as this range shows minimal scatter in the scaling relations (e.g. Kravtsov & Borgani 2012)

* Corresponding author: Charles Romero, romero@iram.fr

owing to the generally low cluster-to-cluster scatter in pressure profiles, found observationally and in simulations, within this radial range (e.g. Borgani et al. 2004; Nagai et al. 2007; Arnaud et al. 2010; Bonamente et al. 2012; Planck Collaboration et al. 2013b; Sayers et al. 2013). While the relative homogeneity of pressure profiles in the intermediate region is well evidenced, it remains important to develop methods to derive non-parametric pressure profiles of clusters so that physical deviations are not artificially smoothed by the adoption of a smooth parametric profile.

This paper is organized as follows. In Section 2 we review the NIKA, MUSTANG, and Bolocam observations and reduction. In Section 3 we address the method used to non-parametrically fit pressure profiles to each of the data sets. Throughout this paper we assume a Λ CDM cosmology with $\Omega_m = 0.28$, $\Omega_\Lambda = 0.72$, and $H_0 = 70 \text{ km s}^{-1} \text{ Mpc}^{-1}$, consistent with the 9-year *Wilkinson Microwave Anisotropy Probe* (WMAP) results reported in Hinshaw et al. (2013).

2. Observations and Data Reduction

2.1. CLJ1226.9+3352

At a redshift of $z = 0.89$, CLJ1226.9+3352, hereafter CLJ 1227, is a massive cluster which was first discovered in the Wide Angle ROSAT Pointed Survey (WARPS Ebeling et al. 2001). It has successively been well studied in the X-ray (*XMM*, *Chandra*, and *XMM/Chandra* Maughan et al. 2004; Bonamente et al. 2006; Maughan et al. 2007, , respectively) and SZ (Joy et al. 2001; Muchovej et al. 2007; Mroczkowski et al. 2009; Mroczkowski 2011; Bulbul et al. 2010; Korngut et al. 2011; Adam et al. 2015). In Maughan et al. (2007), the identification of hot southwestern component gave the first indications of disturbance in this cluster. This interpretation was further bolstered by HST observations (Jee et al. 2009), in which the lensing analysis revealed two distinct peaks, one of which was coincident with the hot X-ray temperature region.

Given the relative circular symmetry of CLJ 1227, it provides a suitable test for determining a non-parametric pressure profile of the cluster, while maintaining the assumption of spherical symmetry. For the centroid, we adopt the X-ray centroid from ACCEPT (Cavagnolo et al. 2009) is at [RA,Dec] = [12:26:57.9,+33:32:49] (J2000). From X-ray data, Mantz et al. (2010) find a scale radius $R_{500} = 1000 \text{ kpc}$, which corresponds to $M_{500} = 12.0 \times 10^{14} M_\odot$.

2.2. NIKA Observations and Reduction

We use in this paper NIKA camera observations of the cluster CLJ 1227, which were obtained at the IRAM 30 m telescope (Pico Veleta) in February 2014 and presented in Adam et al. (2015). NIKA (Monfardini et al. 2010, 2014) was a dual band camera working at 150 and 260 GHz, and made of Kinetic Inductance Detectors (KIDs) operated at 100 mK by using a closed cycle ^3He - ^4He dilution fridge. Furthermore, with a circular field-of-view (FOV) of $1.9'$ ($1.8'$) and a resolution of $18.2''$ ($12.0''$) at 150 (160) GHz NIKA was particularly well adapted to map the thermal Sunyaev-Zeldovich effect in such a high redshift cluster. A detailed description of the performance of the camera can be found in Catalano et al. (2014); Adam et al. (2014).

CLJ 1227 was mapped using on-the-fly raster scans made of either constant azimuth or constant elevation subscans. The

2mm NIKA map, with the point source subtracted (Section 3.1) is shown in the middle panel in Figure 1.

2.3. MUSTANG Observations and Reduction

The MUSTANG camera (Dicker et al. 2008) on the 100 meter Robert C. Byrd Green Bank Telescope (GBT, Jewell & Prestage 2004) with its angular resolution of $9''$ (full-width, half-maximum FWHM) is one of only a few SZ effect instruments with sub-arcminute resolution. However, MUSTANG's instantaneous field of view (FOV) limits its sensitivity to scales larger than $1'$. MUSTANG is a 64 pixel array of Transition Edge Sensor (TES) bolometers arranged in an 8×8 array located at the Gregorian focus on the 100 m GBT. Operating at 90 GHz (81–99 GHz), MUSTANG has an angular resolution of $9''$ and pixel spacing of $0.63 f\lambda$ resulting in a FOV of $42''$. More detailed information about the instrument can be found in Dicker et al. (2008).

Our observations and data reduction are described in detail in Romero et al. (2015), and we briefly review them here. Absolute flux calibrations are based on the planets Mars, Uranus, or Saturn, nebulae, or the star Betelgeuse (α_{Ori}). Responsive detectors are determined by scans taken at regular intervals with a calibration lamp. We fit and subtract a common mode template, polynomial, and sinusoid. Further data quality checks are calculated after this subtraction. The MUSTANG data map, with the point source subtracted (see Section 3.1) is shown in the left panel in Figure 1.

A transfer function was calculated in Romero et al. (2016) when applied to white noise across an entire sky. We find that said transfer function does not fully reproduce the results of a simulated cluster observation. Therefore, we refine the transfer function by filtering a cluster model based on a strictly A10 profile (a gNFW profile with parameters $[\alpha, \beta, \gamma, C_{500}, P_0] = [1.05, 5.49, 0.31, 1.18, 8.42]$) through the standard MUSTANG pipeline and calculate the transfer function. The principle difference between this new transfer function and the former transfer function occurs at scales larger than the FOV (wavenumbers smaller than ~ 0.025 inverse arcseconds).

We verify the fidelity of the new transfer function by reproduce the analysis performed in Romero et al. (2016) for CLJ1227, with the use of the new transfer function in place of the standard MUSTANG filtering procedure. In general, we find good agreement for the constraints on pressure profiles. More specifically, cluster models with $0.5 < C_{500} < 3.3$ are well reproduced with fitted amplitudes that are within 10% of those found in Romero et al. (2016). Furthermore, the best fit profile shape parameters (C_{500} , P_0 , and γ) are within $\sim 10\%$ agreement as well.

2.4. Bolocam Observations and Reduction

To probe a wider range of scales we complement our MUSTANG data with SZ data from Bolocam (Glenn et al. 1998). Bolocam is a 144-element bolometer array on the Caltech Submillimeter Observatory (CSO) with a beam FWHM of $58''$ at 140 GHz and circular FOV with $8'$ diameter, which is well matched to the angular size of R_{500} ($\sim 4'$) of the clusters in our sample.

Bolocam is a 144-element camera that was a facility instrument on the Caltech Submillimeter Observatory (CSO) from 2003 until 2012. Its field of view is $8'$ in diameter, and at 140 GHz it has a resolution of $58''$ FWHM (Glenn et al. (1998);

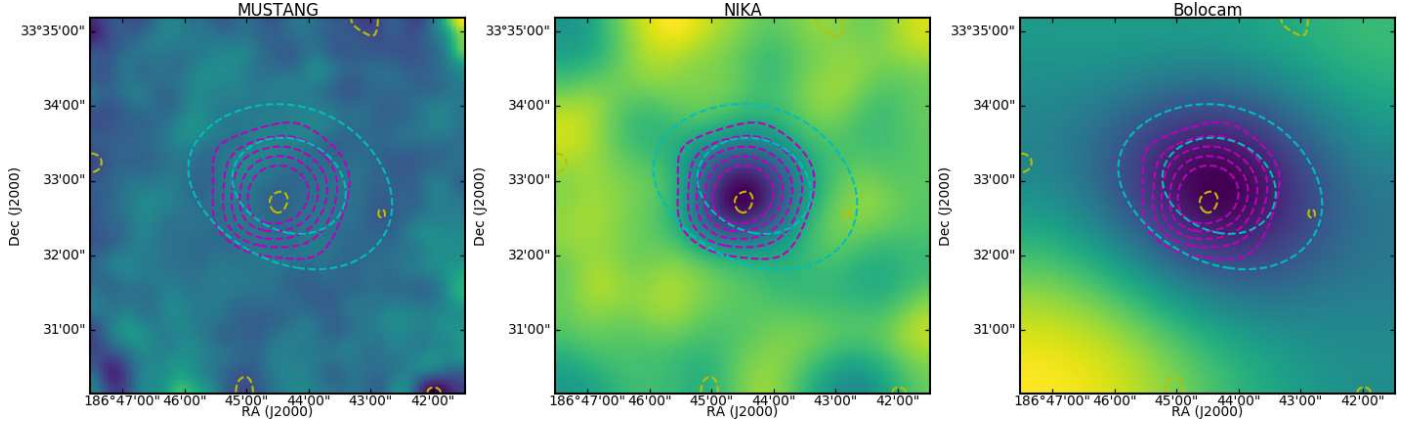


Figure 1. Left: MUSTANG map; Middle: NIKA (2mm) map; Right: Bolocam map. In all three panels, the yellow contours are those of MUSTANG, magenta contours of those of NIKA, and cyan contours are those of Bolocam. For MUSTANG and Bolocam, the contours start at (-2σ) , with 1σ increments. For NIKA, the contours start at (-3σ) with 2σ increments. The point source identified in Adam et al. (2015) is subtracted in the MUSTANG and NIKA maps.

Table 1. Overview of the sensitivities achieved for each of the instruments used in this analysis.

Instrument	Freq. (GHz)	T_{obs} (hours)	Noise (Compton γ)	FWHM ($''$)	FOV ($^{\circ}$)
NIKA	150	7.2	12.5×10^{-6}	18	1.9
MUSTANG	90	4.9	34.2×10^{-6}	9	0.7
Bolocam	150	11.8	8.48×10^{-6}	58	8

Haig et al. (2004)). The clusters were observed with a Lissajous pattern that results in a tapered coverage dropping to 50% of the peak value at a radius of roughly $5'$, and to 0 at a radius of $10'$. The Bolocam maps used in this analysis are $14' \times 14'$. The Bolocam data are the same as those used in Czakon et al. (2015) and Sayers et al. (2013); the details of the reduction are given therein, along with Sayers et al. (2011). The (2mm) Bolocam map is shown in the right panel of Figure 1. The reduction and calibration is similar to that used for MUSTANG, and Bolocam achieves a 5% calibration accuracy and $5''$ pointing accuracy.

2.5. Planck integrated Compton parameter

As in Adam et al. (2015) we consider in the analysis the integrated Compton parameter of the cluster as measured using the Planck data. We use the Planck frequency maps from 143 to 857 GHz to produce a Compton parameter map as described in Hurier et al. (2013) and Planck Collaboration et al. (2013a, 2016). The resolution of this map is $7.5'$, limited by the lowest frequency Planck channel map used in the reconstruction. Using this map we compute the integrated Compton parameter up to a radial distance of $15'$ with respect to the center of the cluster. Uncertainties in the integrated Compton parameter are computed by integrating at random positions around the cluster. The uncertainties obtained have been also cross checked using Planck half-ring half difference Compton parameters obtained as described in Planck Collaboration et al. (2013a, 2016). We find $Y_{15'} = 0.94 \pm 0.36 \times 10^{-3}$ arcmin 2 .

3. Pressure Profiles via Maximum Likelihood

3.1. Preprocessing

A point source at 4.6σ significance in MUSTANG was reported in Korngut et al. (2011), but is not evident in the reprocessed MUSTANG data. A short VLA filler observation (VLA-12A-340, D-array, at 7 GHz) was performed to follow up this potential source, but to a limit of $\sim 50\mu\text{Jy}$ nothing is seen. However, Adam et al. (2015) find a point source at RA 12:27:00.01 and Dec +33:32:42 with a flux density of 6.8 ± 0.7 (stat.) ± 1.0 (cal.) mJy at 260 GHz and 1.9 ± 0.2 (stat.) at 150 GHz. A point source at this location is fit to the MUSTANG data with a flux density of 0.36 ± 0.11 mJy (Romero et al. 2016). We subtract this point source from the NIKA and MUSTANG maps.

The mean level in the MUSTANG map is calculated as the mean within the inner arcminute MUSTANG noise map. We subtract the mean level from the MUSTANG map before fitting a cluster model. The Bolocam map already has a mean level subtracted. The point source is faint enough to not be a concern for the Bolocam data given Bolocam's beam. No mean level is subtracted from NIKA.

3.2. Non-Parametric Models

We employ a spherically symmetric pressure profile as our galaxy cluster model. Our fitting algorithm is applied to each dataset independently; therefore, cluster models are binned and gridded differently for each dataset. Radial bins are defined so that each bin is at least as wide as a beam width, with the additional constraint that the outer most bin is beyond the FOV of the instrument. We define our radial bins based on the radii which confine the bins. Our first bin covers the range $0 < r < R_1$; our second bin covers $R_1 < r < R_2$, and our last (n th) bin covers $R_{n-1} < r$, i.e. it extends to infinity. A finite radius R_n is defined,

and is used to determine the power law in this outermost bin. Pressure normalizations, P_i , are defined at each bin boundary, R_i . We then assume that the pressure in between bin boundaries follows a power law, $P \propto r^{-\alpha}$. We assume that the power law in the first bin is given by the power law of the second bin. The power law of the outermost bin is determined from P_{n-1} (at R_{n-1}) and P_n (at R_n), and extended to infinity. Given the integration along the line of sight, we put a prior on this outer bin such that $\alpha > 1$. We note that under hydrostatic equilibrium (HSE), this should be limited to $\alpha > 3$ in order to avoid having infinite mass.

Given the restrictions of elliptical symmetry and a power law dependence of the integrated quantity (pressure) on the elliptical radius, it is possible to calculate the integral along the line of sight analytically (e.g. Vikhlinin et al. 2001; Korngut et al. 2011). We follow principally the formulation provided in Korngut et al. (2011). As noted in Sarazin et al. (2016), there are certain power laws ($\alpha/2 = p = 1/2, 0, -1/2, -1, -3/2, \dots$) for which the formulation given in Korngut et al. (2011) fails, but a reformulation provides a valid integration. More generally, the formulation fails for $\alpha/2 = p < -1/2$. While a negative index indicates a rise in pressure with radius (atypical), this could arise, especially localised, from shocks, for example. We also wish to minimise our restrictions on the power laws (between bins) so as to minimise induced correlations between bins. Therefore, we implement extensions to the canonical formulation that allow us to integrate within finite regions (spheres or shells that extend only to a finite radius). These extensions and reformulations of specific half integers and described in Section .1.

The integrated profiles, calculated as the Compton y parameter:

$$y = \frac{\sigma_T}{m_e c^2} \int P_e dl, \quad (1)$$

are converted into the units of the original data map. Maps are gridded by assuming a linear interpolation of the 1D (radial) profiles. When gridding our bulk ICM component, we adopt the ACCEP centroid of CLJ 1227. These maps are then convolved with the respective beam and transfer function.

3.3. Fitting Algorithm

We employ a maximum likelihood algorithm, and take our noise to be Gaussian such that our likelihood is given by:

$$\mathcal{L} \propto e^{-\chi^2/2} \quad (2)$$

and χ^2 is given by:

$$\chi^2 = (\vec{d} - \vec{d}_{mod})^T \mathbf{N}^{-1} (\vec{d} - \vec{d}_{mod}), \quad (3)$$

where \vec{d} is our data, \vec{d}_{mod} is our model, and \mathbf{N}^{-1} is our covariance matrix for a given dataset.

In previous works, NIKA and MUSTANG noise has been taken as uncorrelated (e.g. Romero et al. 2015, 2016; Adam et al. 2015). Bolocam noise has been taken as roughly uncorrelated, but 1000 noise realizations, which included CMB and point source estimates, are provided to allow for a more accurate noise estimation (Sayers et al. 2011). We calculate the two-dimensional power spectrum for noise maps of each dataset and find that the noise is consistent with white noise on the scales, for each dataset, which we wish to constrain the models.

We calculate the final probability of our models by applying priors as prescribed by Bayes' Theorem. On each of the pressure bins, we assign strict priors that $P_i > 0$, and as previously mentioned, the last bin has a prior that on its associated power law

slope: $\alpha > 1$. We allow for the choice of including a prior on the integrated Compton Y parameter:

$$Y = \int y d\Omega, \quad (4)$$

where the integral over solid angle taken within a given radius is generally referred to as the cylindrical Compton Y value (Y_{cyl}). We calculate Y_{cyl} using the un-filtered Compton y profile (before convolution with an instrument's beam and transfer function). The prior on Y comes from Planck data (Planck Collaboration et al. 2014). In particular, we take the prior given in Adam et al. (2015): $Y_{cyl}(15') = (0.94 \pm 0.36) \times 10^{-3} \text{ arcmin}^2$.

We employ the described probability function in a python Markov Chain Monte Carlo (MCMC) package, emcee (Foreman-Mackey et al. 2013). This MCMC package makes use of a variant of a Metropolis-Hastings (MH), in particular the ensemble sampling algorithm is affine-invariant (Goodman & Weare 2010). The use of ensemble sampling, as opposed to a canonical single-point sampling, contributes to the notable advantage of this algorithm (within emcee) having a much shorter autocorrelation time than a standard MH algorithm. Furthermore, the computationally expensive part of drawing a new walker has been parallelized.

3.4. Robustness of Fitting Algorithm

Talk about the Virtual fits! This is useful for later section too...

Our non-parametric fits recover consistent pressure profiles given different starting positions and bin spacing. Additionally, we find that our pressure profiles are consistent with those produced when using uniform pressure bins (as opposed to using interpolated power laws). This is true of persistent features, especially those seen at large radii in Bolocam data, where the transfer function shows a notable ringing effect. A drawback of our modelling algorithm is that our requirement that the outer slope be greater than 1 results in our outer two bins, in the Bolocam fits, being affected by the ringing effect, over a wider range of bin spacing.

The outermost bins appear to be affected by systematics from the transfer function, of the respective instrument. Therefore, except for NIKA, where we impose priors to constrain the integrated signal, we do not consider the last bin in further analysis. However, we find that these outermost bins appear important to include within the fitting procedure. In the case of Bolocam, we find the the transfer function appears to also impose a systematic offset on the second-to-last bin as well. Therefore, it too is trimmed.

We find that the use of 6 bins provides generally reliable results. Use of more bins results in larger error bars, while the use of few bins reduces resolution, thereby smoothing out interesting features revealed in our pressure profiles. The results of these fits are shown for NIKA, MUSTANG, and Bolocam in Figures ??, ??, and ?? respectively.

4. Non-parametric Results

Given the MUSTANG transfer function, we expect that the constraints beyond the 42'' (radially) are negligible. Therefore, we exclude the outermost radial bin from further analysis. The Bolocam transfer function is provided as a two-dimensional transfer function. We find that the transfer function produces artifacts at large radii ($r \gtrsim 1000$ kpc) for all plausible cluster models. While we find it important to include these outer bins

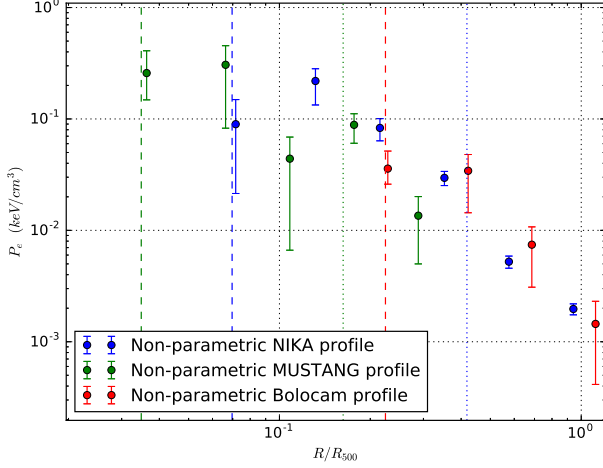


Figure 2. Non-parametric pressure profiles as determined via each dataset individually, and the gNFW (parametric) pressure profile as simultaneously fit to the non-parametric pressure profiles. The error bars are statistical, from the MCMC fits. The vertical dashed and dotted lines correspond to the HWHM and FOV/2 (i.e. radial FOV), respectively; the coloring is also respective to each instrument. The MUSTANG and NIKA points that fall below the gNFW pressure profile (close to $0.1 R_{500}$) are of note and discussed in Section 6.

for the fitting procedure itself, we exclude the outer two points from further analysis.

From the non-parametric chains, we determine a covariance matrix of the pressure bins for each dataset as:

$$\mathbf{N}_{i,j} = \langle d_i d_j \rangle - \langle d_i \rangle \langle d_j \rangle. \quad (5)$$

We show the correlation matrices in Figure 3. We notice that any two adjacent bins are negatively correlated, and by extension, bins spaced 2 apart (e.g bins 1 and 3) are positively correlated. The maximum amplitude of these correlations is 0.05, 0.13, and 0.05 for NIKA, MUSTANG, and Bolocam respectively.

5. Parametric Fits: gNFW

We wish to compare our non-parametric fits to each other and to previous results. Given the ubiquity of parametric pressure profiles, and in particular, the gNFW parameterization, we fit a gNFW profile to our non-parametric pressure profile constraints. The gNFW profile is given as:

$$\tilde{P} = \frac{P_0}{(C_{500}X)^\gamma [1 + (C_{500}X)^\alpha]^{(\beta-\gamma)/\alpha}} \quad (6)$$

where $X = R/R_{500}$, and C_{500} is the concentration parameter; one can also write $(C_{500}X)$ as (R/R_p) , where $R_p = R_{500}/C_{500}$. The exponentials α , β , and γ are commonly cited as the (logarithmic) slopes at moderate, large, and small radii. However, α can be less than γ , or greater than β , without the profile attaining such a slope. Therefore, α should be understood as influencing the rate of turnover between the two slopes, β and γ .

We aim to constrain all parameters within the gNFW profile, but find that α is driven to high values, and furthermore the constraints are very poor for this high values. Therefore, we

choose to restrict α to 1.05, the value found in [Arnaud et al. \(2010\)](#). We further include nuisance parameters of calibration offsets for each dataset. The calibration uncertainties for NIKA, MUSTANG, and Bolocam are taken to be 7%, 10%, and 5% respectively. The mean level in each dataset has already been removed or fitted, so it is not considered here. We use the full covariance matrices from our non-parametric fits.

5.1. Parametric Constraints

We find gNFW parameters of $[P_0, C_{500}, \beta, \text{ and } \gamma] = [42.3^{+13.3}_{-12.5}, 4.85^{+1.27}_{-1.05} \text{ kpc}, 3.12^{+0.31}_{-0.25}, 0.12^{+0.17}_{-0.09}]$. The power law slopes (β and γ) are within expected values given previous gNFW constraints, on CLJ1226 as well as general cluster samples. However, P_0 , and C_{500} are larger than generally found. Given the degeneracy between P_0 and C_{500} , and shape of the pressure profile, these deviations appear to be due to C_{500} being pushed to larger values. A large C_{500} value indicates that the scale radius (transition in pressure profile slope) occurs at a relatively small radius.

We also note that the value of C_{500} itself may not be nearly as high if a smaller value of R_{500} is adopted (implying a smaller M_{500} and P_{500} .) This may well be the case, as several other studies conclude that $R_{500} < 1000 \text{ kpc}$.

6. Discussion

Our non-parametric fits show good reproducibility given different input parameters (Section 3.4). This procedure can be readily applied to elliptical cluster geometries, and could also be modified to include shock components (Appendix). Given the potential for elliptical clusters and presence of shocks, we find that the ability to analyze both the global and local electron pressure in clusters within a non-parametric approach will be of considerable utility as sensitive, high-resolution, SZ observations of individual clusters become more commonplace.

We find generally good agreement in our non-parametric fits between MUSTANG, NIKA, and Bolocam. The fitted gNFW profile reinforces this claim, as all but three points lie within 2.5σ of the fitted curve. The two inner points that fall below the gNFW profile come from MUSTANG and NIKA fits. While neither of their individual deviations is greater than 3σ , their combined significance is greater than 3σ , and given their spatial coincidence, we find it plausible that the deviation is either due to a weak point source or a pressure disturbance in this region.

For NIKA, this deviation occurs in the innermost bin, $r < 17''$, while MUSTANG is able to localize the deviation in a central bin: $9 < r < 23''$. To test the potential for a point source to account for these deviations, we add a point source to the virtual fits mentioned previously (Section 3.4). We run a suite of fits, where we place a point source over the radial range implied by MUSTANG and NIKA, and allow for different flux densities at 90 and 150 GHz. We find that a point source at a radius of $12''$ with flux densities of 0.5 mJy and 1.4 mJy at 90 and 150 GHz roughly reproduces the observed deviations from a gNFW curve.

Given the area enclosed for the MUSTANG and NIKA bins which show this low pressure, such a source would necessarily be $\gtrsim 0.5 \text{ mJy}$ at 90 GHz and 150 GHz. The sensitivity in the MUSTANG and NIKA maps are 0.1 and 0.2 mJy respectively. Such a point source, with its central location, could be masked by the SZ signal in the NIKA map. Indeed, in our simulated images (simulated cluster + point source), the surface brightness at the location of the point source is (1) still negative, and (2) not

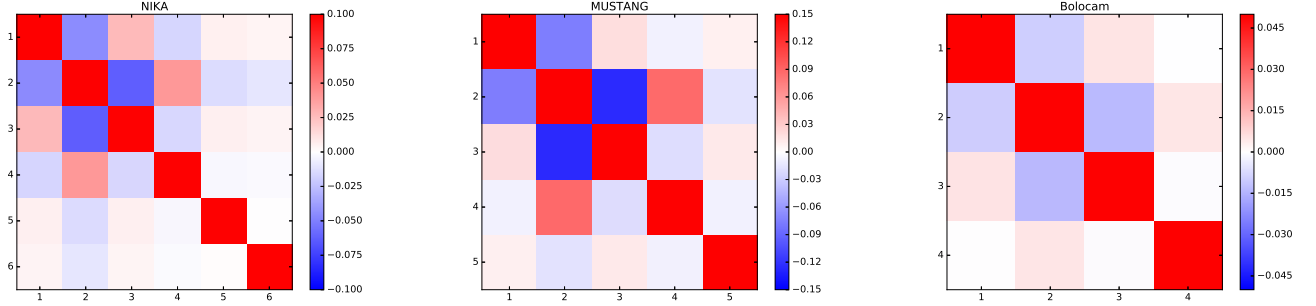


Figure 3. Left: NIKA correlation Matrix. Middle: MUSTANG correlation matrix. Right: Bolocam correlation matrix. The coloring is scaled to make the magnitude of off-diagonal terms more apparent, and the range changes for each instrument.

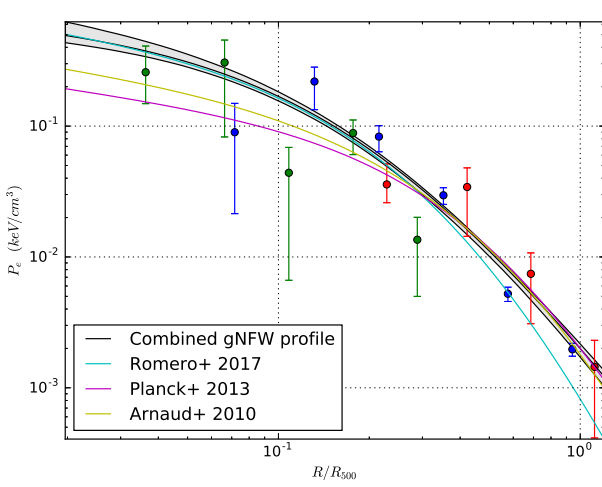


Figure 4. Non-parametric pressure profiles as determined via each dataset individually, and the gNFW (parametric) pressure profile as simultaneously fit to the non-parametric pressure profiles. The error bars are statistical, from the MCMC fits. The vertical dashed and dotted lines correspond to the HWHM and FOV/2 (i.e. radial FOV), respectively; the coloring is also respective to each instrument. The MUSTANG and NIKA points that fall below the gNFW pressure profile (close to $0.1 R_{500}$) are of note and discussed in Section 6.

visually evident to host a point source (perturbation to the smooth surface brightness from the tSZ of the cluster).

The location at $12''$ is well matched to the point source found in Korngut et al. (2011). The potential existence of a point source at this location has already been investigated in the 260 GHz NIKA data (Adam et al. 2015), as well as at lower frequencies and higher frequencies (Section 3.1).

Within our gNFW fits, if α is left unconstrained, we find that large values of α are preferred, indicating a rapid transition between the inner and outer pressure profile slopes. This turnover is largely driven by NIKA, which best covers the spatial region where this transition occurs, and additionally, NIKA has the strongest detection of the cluster and places the greatest constraints on the pressure profile, globally.

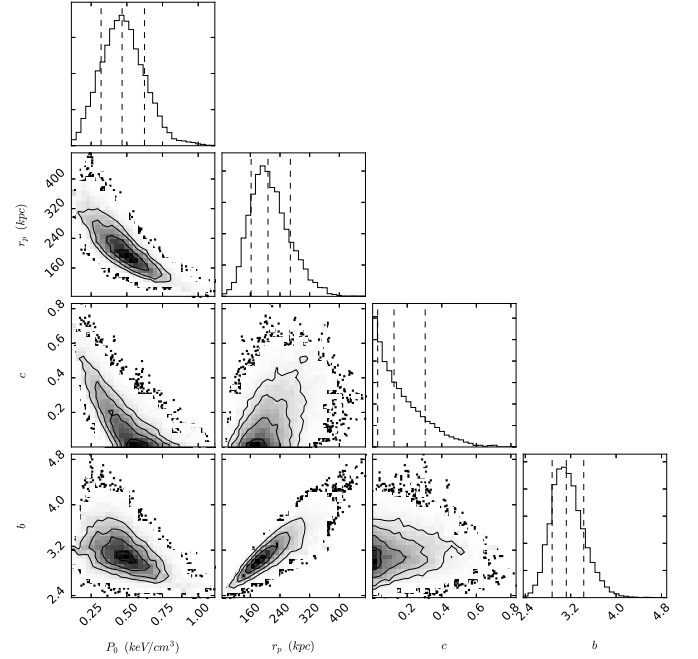


Figure 5. Parameter constraints, P_0 , r_p , γ , and β

6.1. Comparison with Previous SZ Results

From the first SZ measurements of CLJ 1227 (made with BIMA Joy et al. 2001) has generally appeared azimuthally symmetric and relaxed. Later studies with SZA (Muchovej et al. 2007; Mroczkowski et al. 2009; Mroczkowski 2011) all appear to reaffirm this symmetry, while the evidence in SZ observations for a potential disturbance in the core region begins to grow. Korngut et al. (2011) find a ridge of significant substructure in MUSTANG data, which when compared with X-ray profiles, is consistent with a merger scenario within CLJ 1227. However in the current processing of MUSTANG data (Romero et al. 2016), this substructure is not evident. Combining the SZ pressure profile with X-ray electron density profile, Adam et al. (2015) find relatively large entropy values in the core as support for disturbance on small scales. A similar conclusion is reached by Rumsey et al. (2016), who find that the core of CLJ 1227 exhibits signs of merger activity, while the outskirts appear relaxed.

We find that the deviations from a more canonical gNFW pressure profile (e.g. A10 profile) in our non-parametric fits and

parametric fits are consistent with the narrative that the inner region of CLJ 1227 is disturbed. In particular, our non-parametric fits give an indication that the departure from a gNFW profile is marked by a pressure drop at a cluster-centric radius of $\sim 14''$ (~ 100 kpc), where MUSTANG data is critical to determining the location of this pressure deviation.

7. Conclusions

We developed an algorithm to determine a non-parametric pressure profile for galaxy clusters. This method is of particular utility to SZ observations, where the filtering effects from data processing favor model fitting, as opposed to deriving non-parametric pressure profiles via geometric deprojection. Our fitting algorithm is robust with respect to input parameters and bin spacing. While the constraints of single-dish SZ observations beyond the FOV for a given instrument are generally poor, we find that the inclusion of such a bin appears to improve the robustness of the pressure constraints within the FOV.

We find consistency among the non-parametric fits individual instruments, and find that the non-parametric fits indicate a gNFW profile with a relatively small scale radius ($r_p = R_{500}/C_{500}$). If left unconstrained, α tends towards large values, indicating a rapid transition at this scale radius between the inner and outer slope. A significant influence to this transition is the drop in fitted pressure, seen in both MUSTANG and NIKA fits. NIKA is only able to indicate that this drop occurs within the innermost bin, $r < 17''$, while MUSTANG is able to localize it to $9 < r < 23''$. While this drop is only at the $\geq 2.5\sigma$ deviation in MUSTANG and NIKA data, the combined data drop is seen at over 3σ .

Imperical investigations into the potential for point source contamination within this region indicate that such a point source would have to be > 0.5 mJy at both 90 and 150 GHz. This does not provide indication as to whether such a point source is a radio source or DSFG. However, given lower frequency data (VLA, $\sim 50\mu\text{Jy}$ at 7 GHz SZA, 0.2 mJy sensitivity at 30 GHz) and higher frequency data (NIKA 1mm, and Herschel, ?) we find a point source to be an unlikely explanation. Therefore, we find that our data is consistent with a disturbance in the central regions of CLJ 1227.

Given the ability to find deviations from a smooth (parameterized) pressure profile and subsequent flexibility in the application of a non-parametric pressure profile, we believe that such an approach will become more widespread in future SZ studies. The use of (ellipsoidal) shells of pressure, with a power-law dependence, allows for a continuous pressure profile distribution to be analysed. However, such an approach could also be modified to allow for shock modelling (allow for discontinuities) as well. Finally, this approach also allows for some estimation of the pressure profile at very large radii, although such an estimation is highly dependent on the transfer function (i.e. how the raw SZ data is filtered). This is an area of potential improvement, which could come from either how the raw SZ data is filtered, or similarly, how the data is modelled.

Acknowledgements

The National Radio Astronomy Observatory is a facility of the National Science Foundation which is operated under cooperative agreement with Associated Universities, Inc. MUSTANG data was retrieved from . Original MUSTANG data was taken under NRAO proposal IDs GBT/09A-052, GBT/09C-059.

Bolocam data was retrieved from The Bolocam observations presented here were obtained from the Caltech Submillimeter Observatory, which, when the data used in this analysis were taken, was operated by the California Institute of Technology under cooperative agreement with the National Science Foundation. Bolocam was constructed and commissioned using funds from NSF/AST-9618798, NSF/AST-0098737, NSF/AST-9980846, NSF/AST-0229008, and NSF/AST-0206158. Bolocam observations were partially supported by the Gordon and Betty Moore Foundation, the Jet Propulsion Laboratory Research and Technology Development Program, as well as the National Science Council of Taiwan grant NSC100-2112-M-001-008-MY3.

NIKA acknowledgements?

1. Analytic Integrals of Elliptically Symmetric Power Laws

Given the use of the gamma and incomplete beta functions, it is important to recognize its limitations. Specifically, $\Gamma(x)$ is undefined for $x = -i$, $i \in \mathbb{N} \cup \{0\}$ (negative integers, including zero). Furthermore, $x = 0.5 - i$, $i \in \mathbb{N} \cup \{0\}$ is also not calculable here! Finally, all incomplete beta functions are generally defined for $B(x, y)$ that $\text{Re}(x) > 0$ and $\text{Re}(y) > 0$. However, the relation:

$$I_x(a, b) = I_x(a + 1, b) + \frac{x^a(1-x)^b}{aB(a, b)} \quad (.7)$$

allows us to extend our function into the negative domain (for a , which we take as $P - 0.5$).

To deal with the limitation, generally seen as: $2 * x - 2 = -i$, $i \in \mathbb{N} \cup \{0\}$, we derive another approach, from:

$$I = 2\epsilon_0 A^{-2P} \int_0^{\theta_0} (1+t^2)^{-P} c A dt \text{ and now adopt } t^2 = \frac{u}{1-u} \quad (.8)$$

$$= 2\epsilon_0 A^{-2P} \int_0^{\theta_0} (1 + \tan^2(\theta))^{-P} \sec^2(\theta) d\theta \quad (.9)$$

$$= 2\epsilon_0 A^{-2P} \int_0^{\theta_0} \cos^{2P-2}(\theta) d\theta \quad (.10)$$

This must then be extended, and is done so with the relation:

$$\int \cos^{n-2}(\theta) d\theta = \frac{n}{n-1} \int \cos^n(\theta) d\theta - \frac{1}{n-1} \cos^{n-1}(\theta) \sin(\theta) \quad (.11)$$

Given our values of interest/applicability ($2 * x - 2 = -i$, $i \in \mathbb{N} \cup \{0\}$), this extension is perfectly applicable, and we will end in nice functions; either:

$$\begin{aligned} \int \cos^n(\theta) d\theta &= \tan(\theta) \text{ for } n = -2 \text{ or:} \\ \int \cos^n(\theta) d\theta &= \ln |\sec(\theta) + \tan(\theta)| \text{ for } n = -1 \end{aligned}$$

The **only** place where this analytic integration fails is for $p < 0.5$ **when** integrating out to infinity, which is fine, as this must diverge in any case.

References

- Adam, R. et al. 2015, A&A, 576, A12, 1410.2808
- . 2014, A&A, 569, A66, 1310.6237
- Arnaud, M., Pratt, G. W., Piffaretti, R., Böhringer, H., Croston, J. H., & Pointecouteau, E. 2010, A&A, 517, A92, 0910.1234
- Bonamente, M. et al. 2012, New Journal of Physics, 14, 025010, 1112.1599

- Bonamente, M., Joy, M. K., LaRoque, S. J., Carlstrom, J. E., Reese, E. D., & Dawson, K. S. 2006, *ApJ*, 647, 25, arXiv:astro-ph/0512349
- Borgani, S. et al. 2004, *MNRAS*, 348, 1078, astro-ph/0310794
- Bulbul, G. E., Hasler, N., Bonamente, M., & Joy, M. 2010, *ApJ*, 720, 1038, 0911.2827
- Catalano, A. et al. 2014, *ArXiv e-prints*, 1402.0260
- Cavagnolo, K. W., Donahue, M., Voit, G. M., & Sun, M. 2009, *ApJS*, 182, 12, 0902.1802
- Cavaliere, A., & Fusco-Femiano, R. 1978, *A&A*, 70, 677
- Czakon, N. G. et al. 2015, *ApJ*, 806, 18, 1406.2800
- Dicker, S. R. et al. 2014, in *Society of Photo-Optical Instrumentation Engineers (SPIE) Conference Series*, Vol. 9153, Society of Photo-Optical Instrumentation Engineers (SPIE) Conference Series, 0
- Dicker, S. R. et al. 2008, in *Society of Photo-Optical Instrumentation Engineers (SPIE) Conference Series*, Vol. 7020, Society of Photo-Optical Instrumentation Engineers (SPIE) Conference Series, 0907.1306
- Ebeling, H., Edge, A. C., & Henry, J. P. 2001, *ApJ*, 553, 668
- Foreman-Mackey, D., Hogg, D. W., Lang, D., & Goodman, J. 2013, *PASP*, 125, 306, 1202.3665
- Glenn, J. et al. 1998, *Proc. SPIE*, 3357, 326
- Goodman, J., & Weare, J. 2010, *Comm. App. Math. Comp. Sci.*, 5, 65
- Haig, D. J. et al. 2004, in *Society of Photo-Optical Instrumentation Engineers (SPIE) Conference Series*, Vol. 5498, Society of Photo-Optical Instrumentation Engineers (SPIE) Conference Series, ed. C. M. Bradford, P. A. R. Ade, J. E. Aguirre, J. J. Bock, M. Dragovan, L. Duband, L. Earle, J. Glenn, H. Matsuhara, B. J. Naylor, H. T. Nguyen, M. Yun, & J. Zmuidzinas, 78–94
- Hasselfield, M. et al. 2013, *J. Cosmology Astropart. Phys.*, 7, 8, 1301.0816
- Hinshaw, G. et al. 2013, *ApJS*, 208, 19, 1212.5226
- Hurier, G., Macías-Pérez, J. F., & Hildebrandt, S. 2013, *A&A*, 558, A118, 1007.1149
- Itoh, N., Kohyama, Y., & Nozawa, S. 1998, *ApJ*, 502, 7
- Jee, M. J. et al. 2009, *ApJ*, 704, 672, 0908.3897
- Jewell, P. R., & Prestage, R. M. 2004, in *Society of Photo-Optical Instrumentation Engineers (SPIE) Conference Series*, Vol. 5489, Ground-based Telescopes, ed. J. M. Oschmann, Jr., 312–323
- Joy, M. et al. 2001, *ApJ*, 551, L1
- Kitayama, T. et al. 2016, *PASJ*, 68, 88, 1607.08833
- Korngut, P. M. et al. 2011, *ApJ*, 734, 10, 1010.5494
- Kravtsov, A. V., & Borgani, S. 2012, *ARA&A*, 50, 353, 1205.5556
- Mantz, A., Allen, S. W., Rapetti, D., & Ebeling, H. 2010, *MNRAS*, 406, 1759, 0909.3098
- Mason, B. S. et al. 2010, *ApJ*, 716, 739, 0910.5025
- Maughan, B. J., Jones, C., Jones, L. R., & Van Speybroeck, L. 2007, *ApJ*, 659, 1125, astro-ph/0609690
- Maughan, B. J., Jones, L. R., Ebeling, H., & Scharf, C. 2004, *MNRAS*, 351, 1193, astro-ph/0403521
- Monfardini, A. et al. 2014, *Journal of Low Temperature Physics*, 176, 787, 1310.1230
- . 2010, *A&A*, 521, A29, 1004.2209
- Mroczkowski, T. 2011, *ApJ*, 728, L35, 1101.2176
- Mroczkowski, T. et al. 2009, *ApJ*, 694, 1034, 0809.5077
- Muchovej, S. et al. 2007, *ApJ*, 663, 708, arXiv:astro-ph/0610115
- Nagai, D., Kravtsov, A. V., & Vikhlinin, A. 2007, *ApJ*, 668, 1, arXiv:astro-ph/0703661
- Planck Collaboration et al. 2014, *A&A*, 571, A29, 1303.5089
- . 2013a, *ArXiv e-prints*, 1303.5081
- . 2013b, *A&A*, 558, C2
- . 2016, *A&A*, 594, A22, 1502.01596
- Reichardt, C. L. et al. 2013, *ApJ*, 763, 127, 1203.5775
- Romero, C. et al. 2016, *ArXiv e-prints*, 1608.03980
- Romero, C. E. et al. 2015, *ApJ*, 807, 121, 1501.00187
- Rumsey, C. et al. 2016, *MNRAS*, 460, 569, 1604.06120
- Sarazin, C. L., Finoguenov, A., Wik, D. R., & Clarke, T. E. 2016, *ArXiv e-prints*, 1606.07433
- Sayers, J. et al. 2013, *ApJ*, 768, 177, 1211.1632
- Sayers, J., Golwala, S. R., Ameglio, S., & Pierpaoli, E. 2011, *ApJ*, 728, 39, 1010.1798
- Sayers, J. et al. 2016, *ApJ*, 832, 26, 1605.03541
- Vikhlinin, A., Markevitch, M., & Murray, S. S. 2001, *ApJ*, 549, L47, astro-ph/0008499